Journal Pre-proof

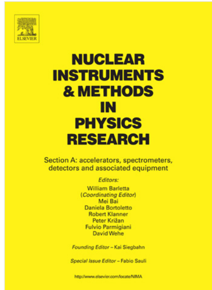

Fragment charge identification technique with a plastic scintillator detector using clinical carbon beams

L. Galli, A.C. Kraan, E. Ciarrocchi, G. Battistoni, N. Belcari, N. Camarlinghi, P. Carra, A. Del Guerra, M. Francesconi, A. Moggi, M. Morrocchi, S. Muraro, M. Pullia, V. Rosso, G. Sportelli, M.G. Bisogni

PII: S0168-9002(19)31461-5
DOI: https://doi.org/10.1016/j.nima.2019.163146
Reference: NIMA 163146

To appear in: *Nuclear Inst. and Methods in Physics Research, A*

Received date : 11 July 2019
Revised date : 18 November 2019
Accepted date : 18 November 2019

Please cite this article as: L. Galli, A.C. Kraan, E. Ciarrocchi et al., Fragment charge identification technique with a plastic scintillator detector using clinical carbon beams, *Nuclear Inst. and Methods in Physics Research, A* (2019), doi: https://doi.org/10.1016/j.nima.2019.163146.

Fragment charge identification technique with a plastic scintillator detector using clinical carbon beams

L. Galli[a,*], A.C. Kraan[a,*], E. Ciarrocchi[b,a,**], G. Battistoni[c], N. Belcari[b,a], N. Camarlinghi[b,a], P. Carra[b,a], A. Del Guerra[b,a], M. Francesconi[b,a], A. Moggi[a], M. Morrocchi[b,a], S. Muraro[c], M. Pullia[d], V. Rosso[b,a], G. Sportelli[b,a], M. G. Bisogni[b,a]

[a] *Istituto Nazionale di Fisica Nucleare, Section of Pisa, Pisa, Italy.*
[b] *Department of Physics, University of Pisa, Pisa, Italy.*
[c] *Istituto Nazionale di Fisica Nucleare, Section of Milano, Milano, Italy.*
[d] *Fondazione CNAO, Pavia, Italy.*

Abstract

Nuclear physics processes are an important source of uncertainty in dose calculations in particle therapy and radioprotection in space. Accurate cross section measurements are a crucial ingredient in improving the understanding of these processes. The FOOT (FragmentatiOn Of Target) experiment aims at measuring the production cross sections of fragments for energies, beams and targets that are relevant in particle therapy and radioprotection in space. An experimental apparatus composed of several sub-detectors will provide the mass, charge, velocity and energy of fragments produced in nuclear interactions in a thin target. A crucial component of the FOOT apparatus will be the ΔE-TOF detector, designed to identify the charge of the fragments using plastic scintillators to measure the energy deposited and the time of flight with respect to a start counter. In this work, we present a charge reconstruction procedure of produced fragments at particle therapy energies. We validate it by measuring the charges of various fragments at an angle of 3.2° and 8.3° with respect the beam-axis, using a small-scale detector and clinical beams of carbon ions at the CNAO oncology center. Experimental results agree well FLUKA Monte Carlo

*These two authors contributed equally to the work.
**Corresponding author

simulations.

Keywords: charge identification, nuclear fragmentation, particle therapy, time-of-flight

1. Introduction

In particle therapy (PT) beams of energetic protons or charged ions are used for cancer treatment. Thanks to the dependence of the energy loss on the velocity of charged particles (Bragg peak), very steep dose profiles can be realized with ion beams, so that the surrounding healthy tissue can largely be spared. At the same time, particle therapy is subject to uncertainties from positioning errors, interplay effects, organ motion, and physics and biological modelling in dose calculations [1]. Especially the value of radiobiological effectiveness (RBE) to correct the physical dose is still under debate (see for instance [2, 3, 4, 5, 6, 7]), demonstrating a complex RBE dependency on dose, cell or tissue type, linear energy transfer and biological endpoints. This, in turn, can translate into an uncertainty in the biological effective dose delivered to the patient.

Nuclear interactions play an important role in RBE variability. In fact, the production of low energy and thus densely ionising fragments can affect the biological effectiveness of the primary beam [6, 8]. In radiobiological-oriented treatment planning systems, these contributions are considered, but with significant uncertainties because they cannot be calculated reliably. A crucial ingredient in the correct modeling of nuclear interaction processes is accurate cross section measurements of particle beams with the human body at therapeutic energies [9, 10]. However, only a limited set of cross section data are available [11, 12]. The goal of the FOOT (FragmentatiOn Of Target) experiment [13] is to provide a new set of cross section measurements for a series of targets and ion beams that are relevant in particle therapy. FOOT aims also at performing charge and mass identification (ID) of the fragments with an accuracy of 3% and 5%, respectively, and at measuring the fragments' energy spectra with an energy resolution of 2 MeV [14]

Target fragmentation measurements are particularly difficult due to the short range (tens of μm) of the recoil nuclei, which have low probability to escape, even a thin target (∼mm), and thus to be detected. To overcome this problem, the FOOT experiment adopts an inverse kinematic approach: ion beams from nuclides abundant in the human body (namely ^{12}C and ^{16}O) are shot onto a hydrogen target to obtain a boost in energy and longer range. In practice, since a pure hydrogen target would be technically difficult to create, measurements are performed with both an hydrogen-enriched target (such as CH_2) and a pure carbon target (graphite), and the proton cross-section is obtained by difference, as done for example in [11].

A scheme and a detailed description of the FOOT apparatus can be found in [13]. Two configurations are foreseen: an emulsion spectrometer, optimized for fragments with $Z \leq 3$ [15], and an electronic setup for higher Z-values ($Z \geq 3$). In the electronic setup, the mass ID is performed by combining the measurements of the momentum, kinetic energy and time of flight (TOF) of the fragment. The charge ID relies instead on the measurements of the energy loss ΔE and of the TOF.

The ΔE-TOF detector is made of two layers of plastic scintillator bars, 3 mm thick, 40 cm long and 2 cm wide. Each bar is optically coupled at both ends to four silicon photomultipliers (SiPM). The bars share a common electronic system for bias, trigger and readout. The two layers are composed of 20 bars each and rotated 90° with respect to each other to provide the coordinates of the crossing fragments. The ΔE-TOF detector is placed at 2 m from the target and the subtended solid angle is ~ 0.04 Sr [16].

During the preparatory phase of the FOOT experiment, the performance of a small-scale ΔE-TOF prototype composed of two bars was assessed as reported in [17]. In the present work, carbon ions impinged onto a 4 mm thick polyvinyl-toluene target (PVT) and the ΔE-TOF prototype was used to detect the fragmentation products. The experimental setup was modeled with a FLUKA Monte Carlo simulation, and the experimental data were compared versus the simulation prediction.

Among the existing works applying charge identification techniques with plastic scintillators, some focus on different energy regimes (see for instance [18, 19]), involving different problematics. In the therapeutic energy range, various fragmentation measurements were reported in the context of non-invasive treatment monitoring [20, 21, 22], however these focused on large opening angles with respect to the beam-axis and allowed to detect only fragments with $Z = 1$. In other studies, various measurements for nuclear fragments are presented for different angles at a few particle energy values [11, 12, 23, 24, 25], and most of these are based on large-scale high-cost experiments.

The goal of the present work is twofold. First, we propose and validate a charge identification procedure for nuclear fragments with the small-scale and low-cost ΔE-TOF detector developed for the FOOT experiment. Second, we show how to apply it by performing charge measurements of fragments produced in a plastic thin target at small angles from the beam-axis. All measurements were performed with carbon ions at the Centro Nazionale Adroterapia Oncologica (CNAO) in Pavia, Italy.

2. Materials and methods

2.1. Experimental setup

A small scale ΔE-TOF detector prototype [17] was realized with two scintillator modules placed at a nominal distance $d = 40$ cm. Each module consisted of a plastic scintillator bar (EJ200, Eljen Technology) of $40 \times 2 \times 0.3$ cm^3, wrapped with reflective aluminum and darkening black tape. Each end of each bar was polished and optically coupled to four SiPMs. Hamamatsu Multi-Pixel Photon Counters with 25 μm cell pitch and 3 mm size were used, corresponding to the scintillator thickness. At each end of each bar, the two series of two SiPMs were connected in parallel. The output signal of each side of each bar was input to a waveform digitiser board, WaveDREAM, hosted in the WaveDAQ integrated trigger and data acquisition system [26, 27]. Each module end was read out by one channel of the WaveDREAM board, that provided also the bias voltage for the SiPMs. The characterisation of the modules has been described elsewhere [17].

The prototype was tested at CNAO in 2018, in two experimental setups, sketched in Fig. 1. The run parameters are summarized in Table 1. In order to cope with electronics dead time, the beam intensity in this setup had to be much lower (order 10^3 Hz) than that in clinical conditions (order 10^8 Hz). For this reason, the accelerator had to be operated in research mode, rather than in clinical mode, implying that the monitoring chambers could not provide information about the number of particles delivered, making it impossible to count the number of initial particles delivered. Only the number of acquired events were counted. In the first setup (Fig. 1a), the modules were irradiated with carbon ions of various kinetic energies per nucleon in the therapeutic range: 115, 190, 260, 300 and 400 MeV/u. Particles were impinging onto the center of the modules.

In the second experimental setup (Fig. 1b), carbon ions were shot on a 4 mm thick target of PVT, and the bars were displaced from the beamline at a specific angle θ, so that fragments from the target could be measured. The beam intensity was of the order of 10^5 Hz. The target was placed at the rotation point, and we have performed measurements in which the center of the bars was at $\theta = 3.2°$ and at $\theta = 8.3°$. The corresponding energy thresholds were 4 MeV

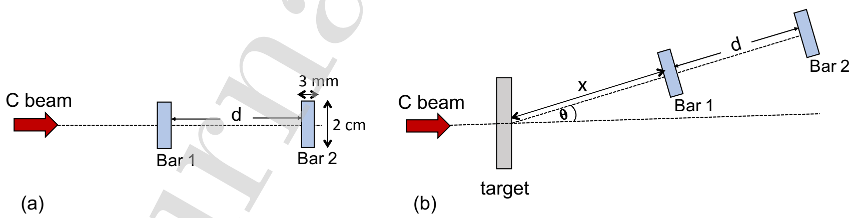

Figure 1: Schematic view (not to scale) of the experimental setups used in this work. (a) Layout for calibration measurements, where the beam was impinging directly onto the bars. (b) Layout for charge identification measurements, where the beam was impinging onto a target and the modules were rotated to $\theta = 3.2°$ and $\theta = 8.3°$. In both cases the nominal distance between the modules was $d = 40$ cm.

Table 1: Summary of run parameters.

Setup	θ [°]	Beam energy [MeV/u]	Target	Data statistics	MC statistics	Energy threshold	d [cm]	x [cm]
Fig. 1a	0	115, 190, 260, 300, 400	No	$2{\cdot}10^4$	10^7	2 MeV	40	40
Fig. 1b	8.3	330	4mm EJ200	$2{\cdot}10^4$	10^8	2 MeV	40	40
Fig. 1b	3.2	280	4mm EJ200	$1{\cdot}10^4$	10^8	4 MeV	40	25

and 2 MeV, respectively. Angles and thresholds were set according to Monte Carlo simulations of the FOOT apparatus performed during the design phase of the experiment [13] and dictated by experimental constraints. Fragments with $Z \geq 3$ are forward emitted within an angle of 5° and with kinetic energy per nucleon around that of the primary beam, while the lighter fragments have a wider angular and kinetic energy distribution. Therefore, while at $\theta = 8.3°$ we expect to observe fragments with $Z < 3$, at $\theta = 3.2°$ we foresee to detect heavier fragments. It must be noted that, being 2 MeV the lowest threshold that can be set above the electronic noise, it resulted in an inefficiency to detect energetic fragments with $Z = 1$ that will be discussed in the next section. The distance between the target and the first bar was $x = 40$ and $x = 25$ cm at $\theta = 8.3°$ and $\theta = 3.2°$, respectively.

In all cases, events were recorded when both modules were triggered. Depending on the beam rate, each measurement was 10-20 minutes long. For all recorded events, an offline data selection was performed, where the difference in energy deposit in both bars was required to be below 5 MeV, to assure that the same fragment was identified. For all events passing this selection, from the collected charge we evaluated the energy deposit ΔE in each bar (see Section 2.3), the TOF between the two bars (see Section 2.4) and the charge Z of the fragments (Section 2.5).

2.2. Monte Carlo simulation

We used the FLUKA Monte Carlo (MC) code [28] to simulate the experimental setups of Fig. 1a and 1b with the run parameters of Table 1. It should be emphasized that, at present, no detector response was included in the simulation, so the results presented below for MC include only the physics of ion-target interactions.

For the first setup (Fig. 1a), monochromatic carbon ions were shot directly on the scintillator modules for various energies and the deposited energy $\Delta E_{i,MC}$ and interaction time $t_{i,MC}$ (where $i = 1, 2$ refers to the module) were recorded. For each energy value, we obtained a distribution of deposited energy in each module, and determined the most probable value (MPV) $\Delta E^{mpv}_{i,MC}$. The TOF of each MC event was defined as $TOF_{MC} = t_{2,MC} - t_{1,MC}$. From the TOF_{MC} distribution we determined the mean value $\mu(TOF_{MC})$. In total we simulated 10^7 events for each energy value.

For the second setup (Fig. 1b), a monochromatic beam of carbon ions were shot on the target. In this case 10^8 events were simulated at each angle. First, a 'clean' selection of events was established, to consider only events with precisely one fragment originating from the target hitting each module, without secondary fragmentation (fragmentation in the module itself). This was useful to study the nuclides that are expected to pass through the bars, and to assure that the charge identification was correct. For these clean events we evaluated the true average velocity in the modules, $\beta_{i,MC}$, as average between the ingoing and outgoing velocities in the modules. We also identified the true nuclides, distinguishing $Z = 1$, 2, 3, 4, 5 and 6. No energy threshold was used here.

Then we performed the same analysis as for data events. First, we selected events that had at least one hit in each module (geometrical cut). The deposited energy $\Delta E_{i,MC}$ (if there was more than one hit, this was the sum of all deposited energies) and the TOF_{MC} (if there was more than one hit, this was the time associated with the first fragment) were registered. Second, an energy threshold was applied of 2 and 4 MeV at $\theta = 8.3°$ and $\theta = 3.2°$, respectively. Third, we required $|\Delta E_{2,MC} - \Delta E_{1,MC}| < 5$ MeV. All the effects of these cuts on the selection efficiency ϵ_{MC} are listed in Table 2. The final selection efficiencies at $\theta = 8.3°$ and $\theta = 3.2°$ were 0.024% and 0.18%, respectively. For all events that passed the selection, we evaluated the Z value as described below in Sec. 2.5.

Table 2: Effects of subsequent selection cuts on the MC simulated events of the setup in Fig. 1b and the irradiation conditions of Table 1.

Cut	ϵ_{MC} at $\theta = 8.3°$	ϵ_{MC} at $\theta = 3.2°$
Fragmentation in target	1.8%	1.8%
Geometrical	6.7%	23%
Energy threshold	97%	83%
$\lvert\Delta E_{2,MC} - \Delta E_{1,MC}\rvert$ <5 MeV	21%	50%
Total efficiency	0.024%	0.18%

2.3. Energy calibration

We used the setup of Fig. 1a to calibrate the energy response of the detector. When charged particles hit a plastic scintillator, scintillation photons are produced. Due to several effects (attenuation, photons exiting the bars on the sides by refraction, absorption depending on the wrapping material), only a fraction of the scintillation photons reaches the photo-detectors at the ends of the scintillator bar, depending on the interaction position. For each event, the total charge $Q_{i,D}$ (where $i = 1, 2$ refers to the module) collected by each module is evaluated from the collected charge (integral of the waveform [16]) on each side $Q_{l,i,D}$ and $Q_{r,i,D}$, where l and r are the left and right side of the bar, respectively, as follows [30]:

$$Q_{i,D} = \sqrt{Q_{l,i,D} \cdot Q_{r,i,D}} \tag{1}$$

The total charge is independent of the particle interaction position. The calibration procedure consists of relating the collected charge $Q_{i,D}$ with a value of deposited energy $\Delta E_{i,D}$. We used the five calibration runs for this purpose, with the setup as described in Fig. 1a and with the run parameters of the first row of Table 1.

For each calibration run, we determined the distribution of collected charge and the MPV of the distribution, $Q^{mpv}_{i,D}$. Moreover, we used the Monte Carlo simulations to determine the distribution of expected deposited energy its MPV, denoted $\Delta E^{mpv}_{i,MC}$ here. We used the MPV, that is less sensitive than the mean, of the charge and energy distribution to avoid the influence of outliers in data. Then the five points were fitted with the function derived from Birk's law [29]:

$$Q_{i,D}^{mpv} = p_{a,i} \cdot \frac{\Delta E_{i,MC}^{mpv}}{1 + p_{b,i} \cdot \Delta E_{i,MC}^{mpv}} \tag{2}$$

where $p_{a,i}$ is a multiplicative term to incorporate the nominal scintillation and detection efficiency, the wrapping, and the optical coupling to the photo-detectors; $p_{b,i}$ is related to saturation effects due to both the scintillator and photo-detectors. For each data event the energy deposited in each detector, $\Delta E_{i,D}$, was obtained by applying the calibration parameters from Eq. 2:

$$\Delta E_{i,D} = \frac{Q_{i,D}}{(p_{a,i} - Q_{i,D} \cdot p_{b,i})} \tag{3}$$

The calibration procedure was applied to each of the five measurements with monochromatic beams, and the energy distributions were obtained. The energy resolution was determined by fitting each energy distribution with a Gaussian function and by evaluating $\mu(\Delta E)$ and $\sigma(\Delta E)$.

2.4. TOF correction

The time-stamp determination of each bar was described in detail in [16, 17], and will be only briefly summarized here. The time stamp $t_{i,D}$ for each bar is determined as the mean value of the time-stamps of each bar end (left and right). This choice allows to remove the dependence of the time information on the interaction position along the bar. For each event, the measured time-of-flight between the two bars, TOF_D, is defined as $TOF_D = t_{2,D} - t_{1,D}$. However, this value still had to be corrected to account for the offset in signal propagation time between the four channels, for instance due to cabling. The correction procedure was similar to the energy calibration, using again the setup of Fig. 1a with the monochromatic ion beams with five energy values. The mean of the measured time of flight distribution, $\mu(TOF_D)$ was evaluated over $2 \cdot 10^4$ events, while the mean of the expected TOF in data was determined from the Monte Carlo simulations, denoted with $\mu(TOF_{MC})$ here. Then we fitted the five points with the following function:

$$\mu(TOF_D) = t_0 + k \cdot \mu(TOF_{MC}), \tag{4}$$

where t_0 accounts for the difference in signal propagation time between the modules, and k accounts for the accuracy in the measurement of the actual distance between the two bars. For each data event we determined the corrected time-of-flight, $TOF_{D,cor}$, by applying the calibration parameters from Eq. 4:

$$TOF_{D,cor} = \frac{TOF_D - t_0}{k} \tag{5}$$

The TOF correction was applied to each of the five measurements with monochromatic beams. To obtain the TOF resolution, the resulting TOF distributions were fitted with a Gaussian function and $\mu(TOF)$ and $\sigma(TOF)$ were evaluated.

2.5. Charge identification

In the energy range relevant for our experiment ($0.1 < \beta < 0.9$), the Bethe-Bloch formula describes the energy loss of a particle as a function of its velocity in the material up to a few percent accuracy:

$$-\frac{dE}{dx} = K \cdot \rho \left(\frac{Z_S}{A_S}\right) \frac{Z^2}{\beta^2} \left[\frac{1}{2} \ln\left(\frac{2m_e c^2 \beta^2 \gamma^2 W_{max}}{I^2}\right) - \beta^2\right] \tag{6}$$

where $K = 0.307$ MeV $\cdot$ mol$^{-1}\cdot$ cm^2, $\rho = 1.023$ g/cm^3 is the scintillator density, $(Z_S/A_S) = 0.5417$ is the ratio of the scintillator atomic and the mass number, Z is the particle charge, $\beta = v/c$ with v the velocity in the scintillator and c the speed of light in a vacuum, $m_e c^2 = 0.511$ MeV is the electron rest mass, $\gamma = \sqrt{1/(1-\beta^2)}$, $W_{max} = 2m_e c^2 \beta^2 \gamma^2$ is the maximum energy transferred in one collision, $I = 64.7$ eV is the scintillator mean excitation potential [31]. We assumed $\frac{dE}{dx} = \frac{\Delta E}{\Delta x}$, where $\Delta x = 3$ mm is the scintillator thickness. We verified that shell and density corrections could be neglected; in fact, these effects are not relevant for the typical fragment velocities in our measurements. Because the velocity of the fragment inside the scintillator is unknown, we used the fragment velocity in between the two modules in Eq. 6, that is a reasonable approximation as the velocities are not too small. Thus, for the MC simulation we estimate the β of the fragment, β_{MC}, as:

$$\beta_{MC} = \frac{d}{c \cdot TOF_{MC}} \tag{7}$$

while for the evaluation of the β of the fragments in data, β_D, we used instead the corrected time-of-flight $TOF_{D,cor}$:

$$\beta_D = \frac{d}{c \cdot TOF_{D,cor}} \tag{8}$$

In our case, where the fragment charge Z is the quantity to be evaluated and the velocity β and the deposited energy ΔE are the measured quantities, we can invert the Bethe-Bloch formula (Eq. 6) to estimate Z for the data and MC simulations:

$$Z = \sqrt{\beta^2 \cdot \frac{\Delta E}{\Delta x} \cdot \left(K \cdot \rho \frac{Z_S}{A_S}\right)^{-1} \cdot \left[\frac{1}{2}\ln\left(\frac{2m_e c^2 \beta^2 \gamma^2 W_{max}}{I^2}\right) - \beta^2\right]^{-1}} \tag{9}$$

Finally, for the data events we fitted the obtained Z distribution with a Gaussian, and extracted the resolution $\sigma(Z)$ and the average $\mu(Z)$.

3. Results

3.1. Energy calibration and time-of-flight correction

In Fig. 2a we show an example of a charge measurement for the experimental setup of Fig.1a, using 190 MeV/u carbon ions. The energy distribution of the corresponding MC simulation is displayed in Fig. 2b, where the value of $\Delta E_{1,MC}^{mpv}$ is indicated with the arrow.

Figure 3a shows the energy calibration procedure for the first module. Here $Q_{1,D}^{mpv}$, the MPV of the charge of the first module, is plotted as a function of the MPV of the expected energy deposited, $\Delta E_{1,MC}^{mpv}$ for the five calibration points. The error bars for the sample standard deviation are smaller than symbols and thus are not shown. The fit with Eq. 2 (red solid line) gave $p_{a,1} = 3.22 \pm 0.01$ MeV^{-1}, $p_{b,1} = (1.41 \pm 0.01) \cdot 10^{-2}$ MeV^{-1}. For the second module, we found $p_{a,2} = 2.76 \pm 0.01$ MeV^{-1} and $p_{b,2} = (1.13 \pm 0.01) \cdot 10^{-2}$ MeV^{-1}. The

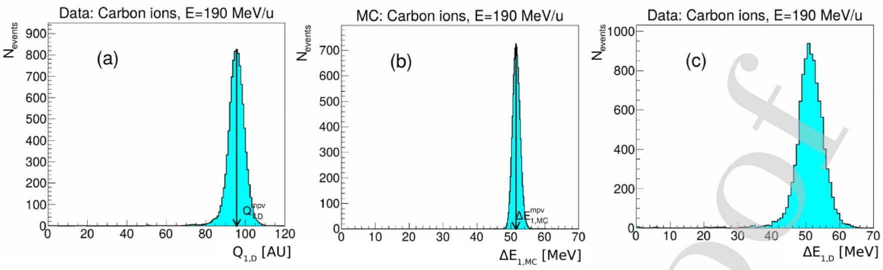

Figure 2: (a) Example of a charge distribution, for carbon ions of 190 MeV/u, where the quantity $Q^{mpv}_{1,D}$ is displayed with the arrow. (b) Distribution of deposited energy in MC simulation for carbon ions of 190 MeV/u, where the quantity $\Delta E^{mpv}_{1,MC}$ is displayed with the arrow. (c) Energy distribution in data resulting after the calibration procedure was applied, for carbon ions of 190 MeV/u.

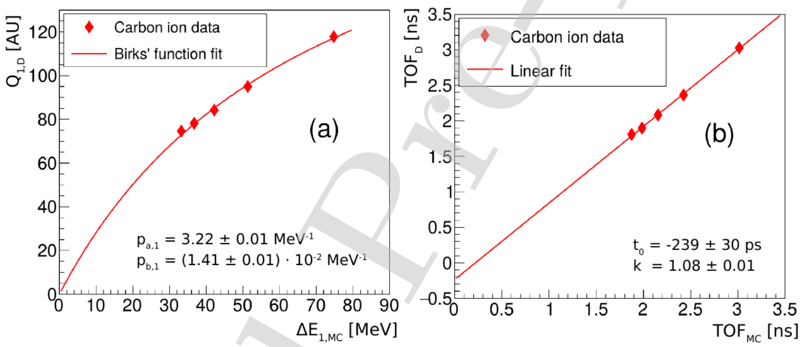

Figure 3: Calibration procedure. (a) Energy calibration: MPV of charge distribution collected by the first bar as a function of the MPV of the expected energy deposited by carbon ions (red diamonds), together with the fit (solid line) with Eq. 2. (b) Mean of the measured TOF as a function of mean of the expected TOF for the five calibration measurements (red diamonds), together with the linear fit (solid line).

differences in p_a and p_b between the two detectors reflect differences in light transport and detection, mainly due to the detector wrapping and coupling to the photo-detectors and to variations in the gain of the photo-detectors. An example of an energy distribution after applying the calibration procedure is given in Fig. 2c.

In Fig. 3b we display $\mu(TOF_D)$ as a function of $\mu(TOF_{MC})$ for carbon ions.

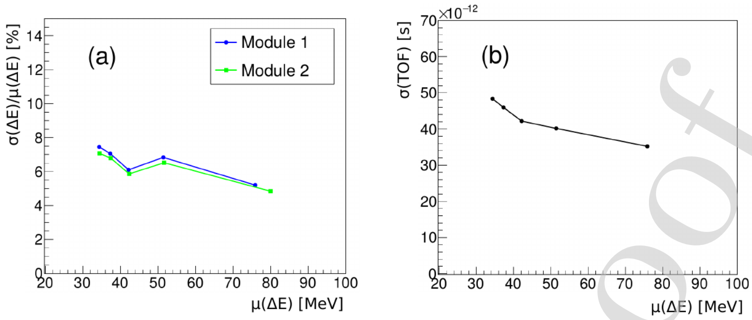

Figure 4: Energy resolution for the two modules (a) and TOF resolution (b) as a function of the mean energy deposit $\mu(\Delta E)$.

The continuous red line is the linear fit (Eq. 4), with coefficient $t_0 = (-239 \pm 30)$ ps, and $k = 1.08 \pm 0.01$. These numbers were used to obtain the corrected time-of-flight in data events, $TOF_{D,cor}$, as written in Eq. 5.

The time and energy resolutions are given in Fig. 4a and 4b, respectively. The energy resolutions for carbon ions of energies ranging from 115 MeV/u to 400 MeV/u were similar in module 1 and 2, and ranged from about 5% to 8%. The TOF resolution ranged from about 35 to 50 ps.

Figure 5 shows the evaluated charge Z of the fragments passing the scintillator for the setup of Fig. 1a, for carbon ions with various energy values impinging onto the scintillator. For the experimental data, the extracted μ and σ values are given in Table 3. The obtained resolution, $\sigma(Z)/\mu(Z)$, is around 3-4%. Resolution effects like fluctuations in the number of produced and detected photons were not included in the MC simulation (see Discussion), explaining the difference in width between MC and data. The MC intrinsic resolution was between 0.7% and 1.8% for energies between 115 MeV/u and 400 MeV/u, respectively. The values of Z are peaked at the carbon charge within 1-2%, confirming that both the energy and time calibrations were correctly performed.

3.2. Fragmentation measurements

Using the experimental setup of Fig. 1b and the beam parameters given in the second and third rows of Table 1, we evaluated the fragments exiting from

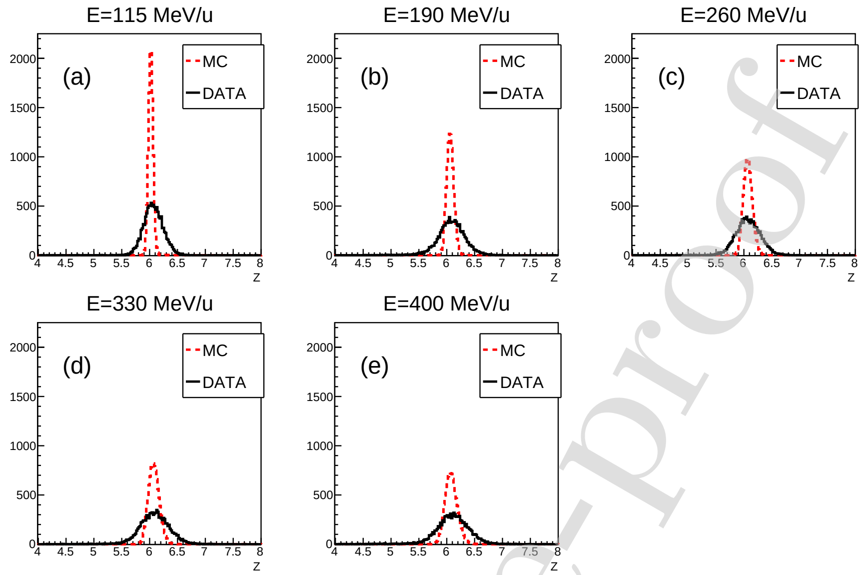

Figure 5: Distribution of reconstructed fragment charge in the first module in data (black solid line) and MC simulation (red dash-dotted line) when the impinging particle are carbon ions, for various energy values. Note that in the MC simulation, no effects of the detector resolution were included.

the target in MC and data. In Fig. 6 for the simulated events passing the 'clean' event selection we display the deposited energy in the first bar, $\Delta E_{1,MC}$, versus $\beta_{1,MC}$ for various charged fragments that are expected to cross the detector at $\theta = 8.3°$ (Fig. 6a) and for $\theta = 3.2°$ (Fig. 6b). The full statistics of the MC simulation was used here. We also display the Bethe-Bloch prediction (solid lines), showing that the fragments follow this trend.

Figure 7 displays the deposited energy in the first module ($\Delta E_{1,D}$ and $\Delta E_{1,MC}$ for data and MC, respectively) as a function of β in between the bars (β_D and β_{MC} for data and MC, respectively), for $\theta = 8.3°$ (Fig. 7a) and $\theta = 3.2°$ (Fig. 7b), for both data (black) and MC (red). The MC distribution was restricted to contain the same total number of entries as the data distribution. The Bethe-Bloch line is also displayed. In Fig. 7a, the events for $Z = 1$ below the Bethe-Bloch line are events where two fragments passed the scintillator bar

Table 3: The values for $\mu(Z)$ and $\sigma(Z)$ for the monochromatic beams.

Beam energy [MeV/u]	$\mu(Z)$	$\sigma(Z)$	$\sigma(Z)/\mu(Z)$ [%]
115	6.06	0.17	2.8
190	6.09	0.22	3.6
260	6.07	0.21	3.5
330	6.09	0.24	3.9
400	6.11	0.26	4.3

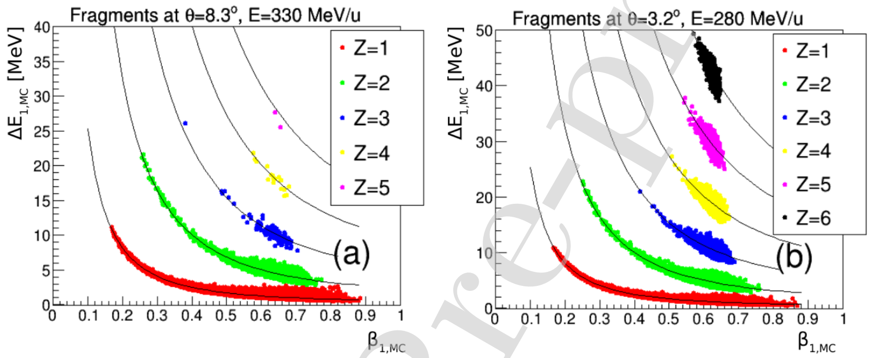

Figure 6: (a) Distribution of deposited energy versus β_{MC} for various nuclides, with the modules were placed at $\theta = 8.3°$ (Table 1 second row). (b) the same, but for $\theta = 3.2°$ (Table 1 third row). The full MC statistics was used in both cases.

simultaneously, resulting in a wrongly correlated time-of-flight and energy deposit. In these cases, the higher energy deposit, belonging to the heavier and slower fragment, is wrongly associated to the smaller TOF, belonging instead to the lighter fragment.

In Fig. 8 we show the evaluated fragment charge Z for $\theta = 8.3°$ (Fig. 8a and 8c) and $\theta = 3.2°$ (Fig. 8b and 8d). A few observations can be made from Fig. 8. First, at $\theta = 8.3°$, only light nuclides with $Z \leq 2$ are detected, while at $\theta = 3.2°$ all possible fragments (except protons, that release an energy under the threshold) are visible. We remind that, for kinematic reasons, the heavier fragments are emitted preferably in the beam direction, while the lighter ones can be emitted at larger angles. Second, no nuclides with $Z > 2$ are shown at

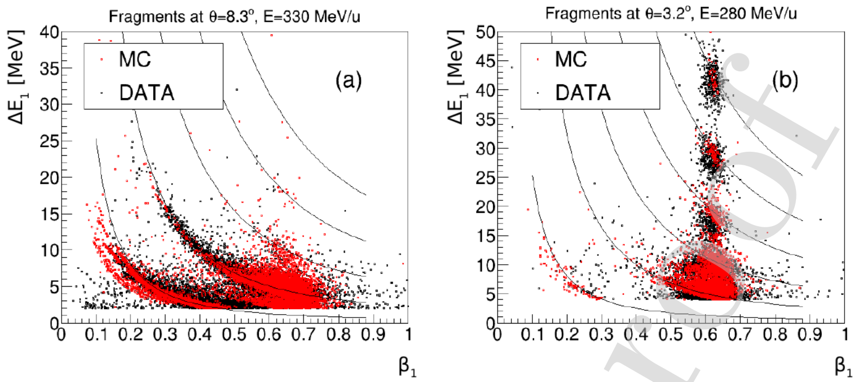

Figure 7: (a) Monte Carlo distribution of deposited energy in the first module versus β (from Eq. 7 and 8), with the modules placed at $\theta = 8.3°$ (Table 1 second row). (b): the same, but for $\theta = 3.2°$ (Table 1 third row). The MC distribution was scaled to have the same number of entries as the data.

$\theta = 8.3°$, while the high statistics simulation (Fig. 6a) predicted the possibility to detect fragments up to $Z = 5$. This is because the statistics of the available data set is not high enough to allow detection of these fragments. Third, at $\theta = 3.2°$, nuclides with $Z = 2, 3, 4, 5$ and 6 can be detected. Although the high statistic simulation (Fig. 6) showed also protons at this angle, the majority of these protons have energy deposits below the threshold of 4 MeV, and, within the statistics of the present data set, hardly any protons could be detected. Figures 8a to Fig. 8d together confirm the ability of the detector to measure all fragment charges up to $Z = 6$.

Table 4 presents the μ and σ resulting from a Gaussian fit of the fragment charge distributions. The distributions are peaked in the correct positions. The resolution on charge reconstruction ranges from 8-9% for lighter fragments ($Z = 1, 2, 3$) to 3-5% for heavier fragments ($Z = 4, 5, 6$). Evaluating the FWHM (2.35σ) of all fits, we see that in most cases FWHM < 0.5 (half the distance between two consecutive peaks), hence the peaks are well separated. The influence of the offline selection cut on $|\Delta E_2 - \Delta E_1|$ (set to 5 MeV) on the values in Table 4 was evaluated by repeating the analyses with cuts of 1 to 10 MeV with

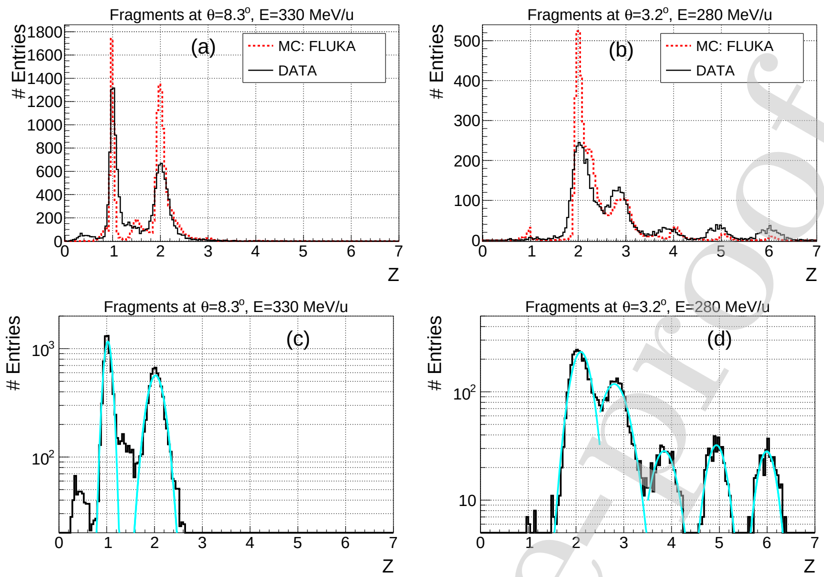

Figure 8: (a) Z of fragments passing through the first module at $\theta = 8.3°$ (Table 1 second row), in data (black solid line) and MC (red dashed line). (b) The same, but for $\theta = 3.2°$ (Table 1 third row). Full statistics was used for the MC distribution, but it was normalized to have the same area as the data. (c) The data distribution from (a) in logarithmic scale including the Gaussian fit (light blue solid line). (d) The data distribution from (b), in logarithmic scale including the Gaussian fit (light blue solid line).

steps of 1 MeV. A cut of 5 MeV gave the best resolution in Z.

Table 4: Results of the Gaussian fit of the Z-peaks for the data.

θ	Energy [MeV/u]	Z	$\mu(Z)$	$\sigma(Z)$	$\sigma(Z)/\mu(Z)$ [%]
8.3°	330	1	1.02	0.08	7.8
		2	2.02	0.17	8.5
3.2°	280	2	2.10	0.20	9.4
		3	2.80	0.27	9.5
		4	3.84	0.23	6.0
		5	4.94	0.19	3.8
		6	5.99	0.18	3.0

4. Discussion

The above work has shown a new charge identification method for the detection of nuclear fragments in particle therapy. Using carbon ion beams at CNAO and a small-scale setup, nuclear fragments with charge from $Z = 1$ up to $Z = 6$ could be successfully detected. This technique can easily be extended to higher energies, that are relevant for radioprotection in space. Some improvements are still possible. First, the systematic effects in Tables 3 and 4 should be better understood. Concerning Table 3, we remind that the Bethe-Bloch formula is accurate only up to a few percent, which could partly explain the systematic effect. However, the deviations in Table 4 for the peaks at $Z = 3$ and $Z = 4$ are larger. This issue is currently under investigation. It is possible that the relationship in Eq. 2 depends on the ion type and that the calibration curve in Fig. 3 does not perfectly hold for all ions. Calibration measurements with different ions are foreseen in the future to clarify this issue. Second, the MC distributions did not include a full simulation of all experimental issues. In fact, the width of the Z distributions in data is much wider than in MC (see Fig 5 and Fig. 8), mainly due to statistical fluctuations in the number of produced and detected scintillation photons. A minor role is attributed to the SiPM crosstalk, after-pulse and electronic noise. Future work includes a full simulation or parameterization of all these effects. Finally, there are other aspects that could influence the Z resolution, like secondary fragmentation (fragmentation in the bar), the influence of double hits in the detector, etc. All these aspects are currently under investigation.

In the context of the FOOT experiment, we believe the performance of the prototype is satisfactory and the modules can be used for the construction of the full-scale ΔE-TOF detector. Future work will include the assembling and testing of such a detector, that is designed to be made of two layers of 20 orthogonally oriented plastic scintillator modules.

Apart from the validation of a charge identification procedure, the work presented here is also an example of how valuable nuclear interaction data can be obtained with relatively simple, small and low-cost setups, allowing any particle therapy center to perform such measurements. It can easily be extended to other angles and other energies. Such fragment charge measurements are useful for the validation of nuclear physics models in Monte Carlo codes.

5. Conclusion

In this study we have presented a new charge identification procedure for nuclear fragments in particle therapy, using a small scale ΔE-TOF prototype detector, in preparation for the FOOT experiment. It was validated at CNAO with monochromatic carbon ion beams that were shot directly on the bars, and it was used to detect nuclear fragments at angles of 3.2° and 8.3° with respect to the beam-axis, produced by irradiating a thin plastic target with carbon ions of 280 MeV/u and 330 MeV/u, respectively. At 3.2° we detected fragments from $Z = 2$ up to $Z = 6$, while fragments with $Z = 1$ were not detected because of the energy threshold in the experimental setup. At 8.3° we detected fragments with $Z = 1$ and $Z = 2$. The resolution on charge reconstruction ranges from 8-9% for lighter fragments ($Z = 1, 2, 3$) to 3-6% for heavier fragments ($Z = 4, 5, 6$), however confirming the capability of disentangling different charged fragments.

The above work is an example of how valuable measurements can be obtained with simple and small experimental setups in clinical settings, helping to improve the understanding of nuclear interaction processes. Moreover, it represents an important step forward in the design and construction of the FOOT apparatus, bringing us closer towards a new large set of highly relevant measurements for therapeutic and space radioprotection purposes.

Acknowledgements

We thank Sandro Bianucci, Alessandro Profeti and Alessandro Soldani for their technical support.

References

[1] J.S. Loeffler, M. Durante. Charged particle therapy–optimization, challenges and future directions. Nat. Rev. Clin. Oncol. 10(7): 411 (2013). doi:10.1038/nrclinonc.2013.79.

[2] L.E. Gerweck, S.V. Kozin. Relative biological effectiveness of proton beams in clinical therapy. Radiother. Oncol. 50(2): 135-142 (1999). doi:10.1016/S0167-8140(98)00092-9.

[3] H. Paganetti. Relative biological effectiveness (RBE) values for proton beam therapy. Variations as a function of biological endpoint, dose, and linear energy transfer. Phys. Med. Biol. 59(22): R419-R472 (2014). doi:10.1088/0031-9155/59/22/R419.

[4] M. Durante, H. Paganetti, A. Pompos, S.F. Kry, X. Wu, D.R. Grosshans, Report of a National Cancer Institute special panel: Characterization of the physical parameters of particle beams for biological research. Med. Phys. 46(2): e37-e52, (2019). doi:10.1002/mp.13324.

[5] K. Ilicic, S.E. Combs, T.E. Schmid. New insights in the relative radiobiological effectiveness of proton irradiation. Radiat. Oncol. 13(1): 6 (2018). doi:10.1186/s13014-018-0954-9.

[6] F. Tommasino and M. Durante. Proton Radiobiology. Cancers 7(1): 353-381 (2015). doi:10.3390/cancers7010353.

[7] O. Mohamad, B.J. Sishc, J. Saha, et al., Carbon ion radiotherapy: a review of clinical experiences and preclinical research, with an emphasis on DNA damage/repair. Cancers 9(6): 66 (2017). doi:10.3390/cancers9060066.

[8] N. Matsufuji, A. Fukumura, M. Komori, T. Kanai, T. Kohno, Influence of fragment reaction of relativistic heavy charged particles on heavy-ion radiotherapy. Phys. Med. Biol. 48(11): 1605-1623 (2003). doi:10.1088/0031-9155/48/11/309.

[9] G. Battistoni, et al., The FLUKA code: an accurate simulation tool for particle therapy. Front. Oncol. 6: 116 (2016). doi:10.3389/fonc.2016.00116.

[10] L. Walsh, U. Schneider, A. Fogtman, et al., Research plans in Europe for radiation health hazard assessment in exploratory missions. Life Sciences in Space Research 21: 73-82 (2019). doi:10.1016/j.lssr.2019.04.002.

[11] J. Dudouet, D. Juliani, M. Labalme, et al., Double-differential fragmentation cross-section measurements of 95 MeV/nucleon 12 C beams on thin targets for hadron therapy. Phys. Rev. C 88(2): 024606 (2013). doi:10.1103/PhysRevC.88.024606.

[12] M. Toppi, Z. Abou-Haidar, C. Agodi, et al., Measurement of fragmentation cross sections of ^{12}C ions on a thin gold target with the FIRST apparatus. Phys Rev C 93(6): 064601 (2016). doi:10.1103/PhysRevC.93.064601.

[13] V. Patera et al., The foot (fragmentation of target) experiment. The 26th International Nuclear Physics Conference 281: 128. SISSA Medialab (2017). doi:10.22323/1.281.0128.

[14] S. Valle, Design, simulation and performances study of the FOOT experiment, PhD thesis, Università degli Studi di Milano (2018).

[15] M.C. Montesi, A. Lauria, A. Alexandrov, et al., Ion charge separation with new generation of nuclear emulsion films. Open Phys. 17(1): 233-240 (2019). doi:10.1515/phys-2019-0024.

[16] M. Morrocchi, E. Ciarrocchi, A. Alexandrov, et al., Development and characterization of a ΔE-TOF detector prototype for the FOOT experiment. Nucl. Instrum. Methods Phys. Res. A 916: 116-124 (2019). doi:10.1016/j.nima.2018.09.086.

[17] E. Ciarrocchi, N. Belcari, N. Camarlinghi, et al., The ΔE-TOF detector of the FOOT experiment: Experimental tests and Monte Carlo simulations. Nucl. Instrum. Methods Phys. Res A 936: 78-79 (2019). doi:10.1016/j.nima.2018.08.117.

[18] P.S. Marrocchesi, O. Adriani, Y. Akaide, et al., Beam test performance of a scintillator-based detector for the charge identification of relativistic ions. Nucl. Instrum. Methods Phys. Res. A 659(1): 477-483 (2011). doi:10.1016/j.nima.2011.08.034.

[19] T. Dong, Y. Zhang, P. Ma, et al, Charge measurements of cosmic ray nuclei with the plastic scintillator detector of DAMPE. Astropart. Phys. 105: 31-36 (2019). doi:10.1016/j.astropartphys.2018.10.001.

[20] K. Gwosch, B. Hartmann, J. Jakubek et al., Non-invasive monitoring of therapeutic carbon ion beams in a homogeneous phantom by tracking of secondary ions. Phys. Med. Biol. 58: 11 (2013). doi:10.1088/0031-9155/58/11/3755.

[21] C. Agodi, G. Battistoni, F. Bellini, et al., Charged particle's flux measurement from PMMA irradiated by 80 MeV/u carbon ion beam. Phys. Med. Biol. 57(18): 5667 (2012). doi:10.1088/0031-9155/57/18/5667.

[22] L. Piersanti, F. Bellini, F. Bini, et al., Measurement of charged particle yields from PMMA irradiated by a 220 MeV/u 12C beam. Phys. Med. Biol. 59(7): 1857-72 (2014). doi:10.1088/0031-9155/59/7/1857.

[23] N. Matsufuji, M. Komori, H. Sasaki, et al., Spatial fragment distribution from a therapeutic pencil-like carbon beam in water. Phys. Med. Biol. 50(14): 3393-403 (2005). doi:10.1088/0031-9155/50/14/014.

[24] E. Heattner, H. Iwase, D. Schardt, Experimental fragmentation studies with ^{12}C therapy beams, Radiat. Prot. Dosimetry 122(1-4): 485-487 (2006). doi:10.1093/rpd/ncl402.

[25] K. Gunzert-Marx, H. Iwase, D. Schardt, R.S. Simon, Secondary beam fragments produced by 200MeVu1 12C ions in water and their dose contributions in carbon ion radiotherapy. New J. Phys. 10(7): 075003 (2008). doi:10.1088/1367-2630/10/7/075003.

[26] L. Galli, A. Baldini, M. Cei, et al., WaveDAQ: An highly integrated trigger and data acquisition system. Nucl. Instrum. Methods Phys. Res. A 936: 399-400 (2019). doi:10.1016/j.nima.2018.07.067.

[27] S. Ritt, R. Dinapoli, U. Hartmann, Application of the DRS chip for fast waveform digitizing. Nucl. Instrum. Methods Phys. Res. A 623(1): 486-488 (2010). doi:10.1016/j.nima.2010.03.045

[28] A. Ferrari, et al., FLUKA: a multi-particle transport code. CERN-2005-10, INFN TC 05/11, SLAC-R-773 (2005).

[29] J. B. Birks, The theory and Practise of Scintillation Counting, Pergamon Press, Oxford (1964).

[30] G.F. Knoll, Radiation detection and measurement. Fourth Edition, John Wiley and Sons (2010).

[31] http://pdg.lbl.gov/2018/AtomicNuclearProperties/HTML/polyvinyltoluene.html (accessed on 2019/11/12)